ORIGINAL ARTICLE

Application of laser-induced thermal acoustics in air to measurement of shock-induced temperature changes

Toshiharu Mizukaki · Toyoki Matsuzawa

Abstract The laser-induced thermal acoustics (LITA) method was used to measure the temperature profiles induced behind spherical shock waves, generated by high-voltage discharge in air with an energy of 6 J. A Nd:YAG laser (wavelength 532 nm, energy 300 mJ, pulse duration 10 ns, line width $0.005 \, \text{cm}^{-1}$) and an Ar-ion laser (wavelength 488 nm, power 4 W) served as the pump and probe lasers, respectively for the LITA measurements. The peak temperatures were in good agreement with results calculated with the Euler equations. The temperature profiles behind the shock, however, differed in decay rates. The peak temperatures behind the shock wave were determined by reflected overpressure and agreed with those from the LITA measurements within a maximum error of 5%.

Keywords Laser-induced thermal acoustics · Shock-induced temperature · ESWL

PACS 47.80.-v · 42.25.Fx · 47.35.Rs

1 Introduction

For the last two decades, high pressure generated by underwater shock wave focusing, has been successfully applied to noninvasive disintegration of human calculi called

T. Mizukaki (✉)
Department of Astronautics and Aeronautics,
Tokai University, 1117 Kitakaname, Hiratsuka 259-1292, Japan
e-mail: mizukaki@keyaki.cc.u-tokai.ac.jp

T. Matsuzawa
Technical Research and Development Institute,
Ministry of Defense, 2-1-1 Nakameguro, Tokyo 153-8630, Japan

extra-corporeal shock wave lithotripsy (ESWL) [7]. This basic research has successfully been extended to clinical applications. It has been found, however, that despite clinical success, tissue damage, although not very serious, occurs during ESWL treatment. Clarifying the mechanism of tissue damage from heat, which is induced by underwater shock wave focusing, the temperature profile near the focusing point requires experimental investigation, with high-temporal resolution that requires a response frequency greater than 1 MHz. The first application of micro explosives to ESWL was reported by Kuwahara et al. [23]. Ioritani [15] revealed that there is neither a pressure range nor a number of shock repetitions at which human calculi are selectively disintegrated without causing tissue injury. Takayama summarized an ESWL-development research project, and briefly described a possible mechanism of tissue damage during ESWL [29]. The reports on temperature changes induced by shock focusing, however, are the results of numerical analysis, rather than experimentation. Thus, the mechanisms of tissue damage from temperature remain largely unknown.

There is a growing interest in the utilization of plasmas in aerodynamics, particularly for high-speed flow applications. Investigation in the utilization of plasmas for aerodynamic research was initiated by the experiments of Klimov et al. [17], who demonstrated that the strength of a propagating normal shock is reduced in the presence of a weakly ionized flow. Also initial experiments by Gordeev et al. [12] suggested that aerodynamic drag can be significantly reduced by initiating a plasma in front of a body placed in supersonic flow. Even though much research has been conducted suggesting that the mechanism for these effects was mostly thermal instead of electromagnetic, there is still a variety of applications where plasmas can be used for aerodynamic flow control [26]. These aerodynamic applications generally utilize continuous or pulsed plasmas that have been

initiated by microwaves or by laser-induced optical break-down. Applications of plasmas for aerodynamic flow control include control of large-scale structures in compressible shear layers [2,5], creation of virtual cowl inlets [24], creation of virtual thermal fore bodies for sonic boom reduction [25], and control of shock waves and their interactions [1,3,21,26,31,32]. Even though many reports on fundamental research of flow control with energy deposition have been published, none of the demonstration devices has appeared. Adelgren et al. [1] have observed the evolution of the plasma generated by laser optical breakdown to investigate the interaction of energy deposition with supersonic flow. They have reported that energy deposition caused the displacement of the Mach disk inside under-expanded jets and the decrease of static pressure on the surface of spheres behind bow shocks. Satheesh et al. [27] have succeeded in demonstrating a drag reduction of 50% for a blunt body in hypersonic flow by arc discharges introduced upstream of bow shocks. Glumac et al. [10] applied the filtered Rayleigh scattering method for remote thermometry to evaluate shock strength generated by laser optical breakdown. The method can spectroscopically measure plasma temperature reaching into the tens of thousands Kelvin. Specifically, the method measures the two-dimensional spectrum of Rayleigh scattering coming from a sheet-laser beam irradiated in the test section. The spectrum was obtained with a high-speed intensified-CCD camera and extracted two-dimensional temperature information from inside the plasma. The temperature information allows us to estimate the strength of spherical shock waves generated by plasma evolution. Glumac et al. showed that the filtered Rayleigh scattering method was suitable to obtain the temperature history and profile inside a developing plasma, however, the method did not give the solution for temperature measurement behind propagating shock waves.

The temperature changes induced by propagating shock waves are unsteady phenomena, with a duration of tens of microseconds. Thus, accurate temperature measurements require resolution of more than 1 MHz to obtain an accurate history of the temperature changes. Most thermocouples are not suitable for these measurements because of their 1 kHz temporal resolution. Although recently developed thin-film thermocouples [20] have reported temporal resolution of 1MHz, these thermocouples are not designed to measure the temperature of free space, instead of that of the surface of a test model in a hypersonic wind tunnel. Thus, a temperature-measurement technique, which is both non-intrusive and has a high frequency response is needed to obtain the history of shock-induced temperature. Several reports [4,11] describe applications of laser-induced thermal acoustics (LITA) for thermometry for distilled water. None of the reports, however, has reported dynamic temperature measurement.

Laser-induced thermal acoustics (LITA) has been applied to advanced velocimetry for wind tunnel experiment [13,14,

22,28,30]. LITA can provide non-invasive determination of the speed of sound in a medium. Moreover, the advantages of LITA over other fluid measurement techniques using reference particles such as PIV and LDV, are short duration (sub-microsecond measurement duration) small test volume (sub-millimeter diameter), and particle-free. We applied LITA to thermometry for shock-induced temperatures. In this paper, we have obtained shock-induced temperatures in air as a preliminary step toward thermometry for underwater-shock-induced temperatures because the ratio of shock-induced temperature change in air is larger than in water. The results of temperature measurements carried out behind spherical shock waves are described in this paper.

2 Experimental setup

2.1 Shock wave generator and visualization

Spherical shock waves generated by high-voltage discharges (a total energy of 6 J and 300 ns spark duration) were employed to generate the steep and dynamic temperature changes examined here. The high-voltage discharges were generated with a shock generator (MONOFLASH, High-Speed Photo-System, Inc.). This device was originally designed as a light source. Figure 1 shows the dimensions of the shock wave generator and the location of the test volume for temperature measurement. The distance of the test volume x from the generator ranged from 30 to 60 mm in 10 mm intervals. Shock-induced overpressure was measured with a piezoelectric pressure transducer (PCB M105C22) to estimate the temperature behind the shock waves. We also required the $x-t$ diagram of the generated shock wave to synchronize irradiation of the lasers with shock waves passing through the test volume. Optical flow visualization was carried out to obtain the locations of the generated shock front. The dissection-color Schlieren method [8,18] was used for the visualization. Referring to the obtained $x-t$ diagram, we determined the delay time of the laser irradiation. The optical setup included two Schlieren mirrors with an effective diameter of 500 mm and a focal length of 5 m. A high-intensity, short-duration Xenon spark flash (NANOSPARK-4000P, BIOLEK) served as the light source. The light source had spark duration of less than 1 μs. The images were recorded with a digital still camera (D1x, NIKON) that had a CCD with 4,048 × 1,324 pixels and an imaging lens with a 200 mm focal length.

2.2 LITA-thermometry setup

The experimental arrangement is shown schematically in Fig. 2. The two grating excitation beams, with wavelength of 532 nm, were provided by a pulsed Nd:YAG laser. The pulse length of the laser is about 10 ns, and the spectral bandwidth

Fig. 1 Shock wave generator
and test volume

(a) Front view   **(b)** Side view

(c) Arrow view A-A
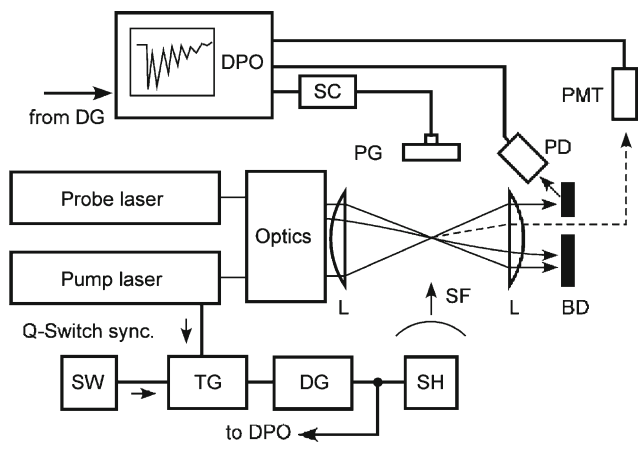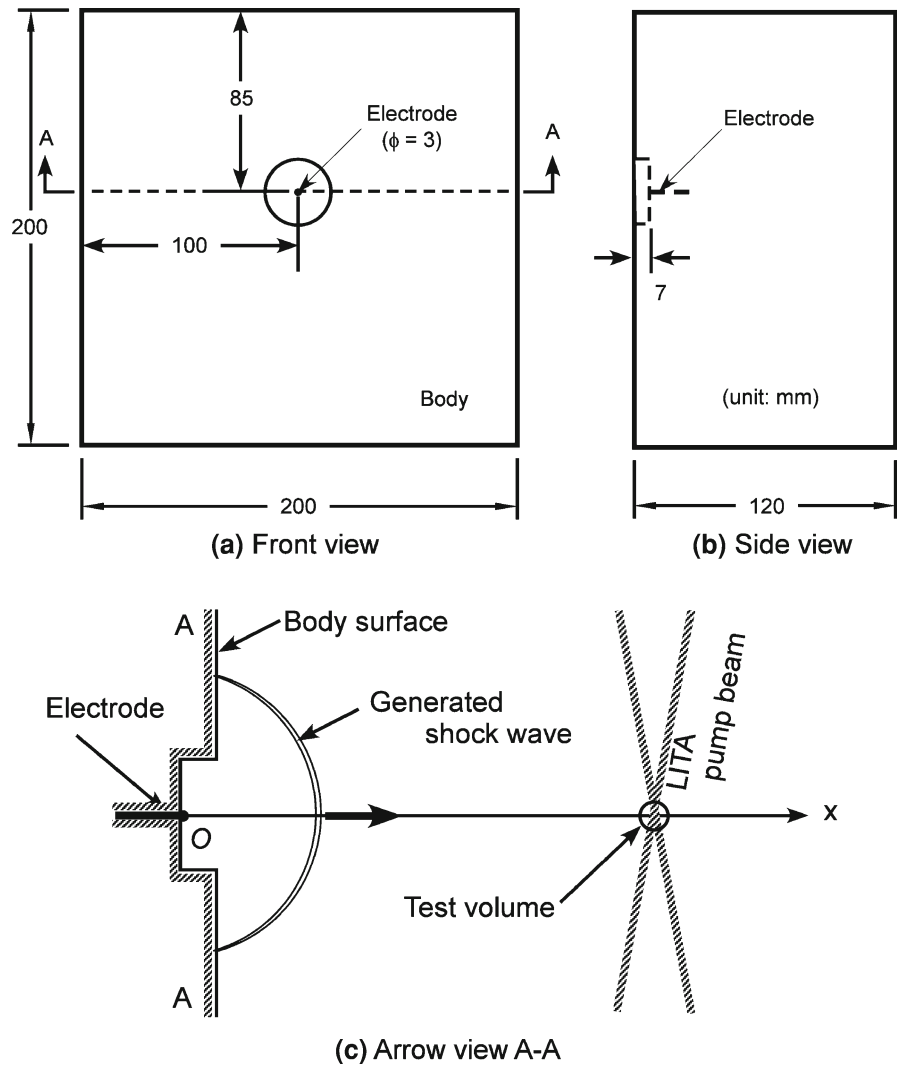
Fig. 2 Schematic diagram of LITA thermometry

of the radiation has a FWHM of less than $0.005 \, \mathrm{cm^{-1}}$. The output energy of the laser is about 300 mJ/pulse. The diameter of the laser beams was approximately 10 mm each. The irradiated beam from the laser was divided into two beams with a half mirror, and then turned them parallel with plane mirrors. Those parallel beams were converged with a focusing lens (L) with a focal length of 800 mm and a diameter of 100 mm. At the focus point of the focusing lens, in this experiment, the half-crossing angle of the beams θ was 0.426°. Beyond the focusing point, the beams become parallel again with another focusing lens with the same specification as the previous one so that a beam-dumper (BD) can capture one of them, and a photo detector (PD) could detect the other. The signal from the PD served as trigger signal to initiate measurement. The laser-induced grating is read out by the beam of a cw Ar^+ laser, operated at 488 nm with a power of approximately 2.5 W. The cw Ar^+ laser beams had a diameter of approximately 2 mm. The beam was set to a phase-match geometry at the focusing point, with both mirrors and lenses. A half-crossing angle $\psi = 0.391°$ was employed for the phase-match condition. The beam was captured at the BD after passing L. Both a narrow-band interference filter,

with FWHM of 10 nm for a wavelength of 488 nm, and a spatial filter reduced the noise light in the beam before insertion into a photo multiplier (PMT, Hamamatsu H6780). The PMT detected the beam through an optical fiber. The intensity history of the beam was recorded and stored with a high-speed digital oscilloscope (DPO, 20 GSa, 2.5 GHz, Tektronix TDS7254). A switch box (SW) generated the measurement-activation signal. A trigger generator (TG) initiated a main trigger signal immediately after detecting both the activation signal and the Q-switch-synchronize signal generated by the pump laser. A delay generator (DG) added a time-delay to the main trigger signal to synchronize shock wave generation with the laser irradiation. The shock wave generator (SH) generated shock waves. The DPO recorded the main trigger signal to determine the moment of shock generation. The overpressure history caused by the shock waves was obtained with a piezo-electric pressure transducer (PG) through a signal conditioner (SC). The crossing beams form a spindle-shaped test volume. The propagation direction of the generated spherical shock wave was parallel to the minor axis of the test volume. Lengths of the major axis l and the minor axis m are $4d/\sin\theta$ and $4d/\cos\theta$, respectively. In the present experiment, both values were estimated to be 27.9 mm and 208 μm. Where beam waist $d = 1.22 \cdot \lambda \cdot f/w_0$, wavelength of the pump beam λ, focal length of the converging lens f, and diameter of the pump beam at the converging lens $w_0 = 5$ mm. Initial diameter of the pump beam, 10 mm, was reduced by an aperture diaphragm before passing the converging lens. The resulting values of the temperature obtained from LITA measurement are averaged values of the temperature over the test volume. Accuracy improvement in the resulting temperature would be achieved by: (1) increasing the crossing angle θ, (2) decreasing the wavelength of the pump laser λ, and (3) decreasing the focal length of the converging lens f. The smaller volume, however, gives a shorter duration LITA signal, which provides low accuracy. Good accuracy with the smaller test volume requires a pump laser with ultra-short duration such as pico-second pulsed lasers [4].

2.3 Temperature determination from LITA signal

On the basis of the theory presented in the literature [9], the oscillation period of the diffraction efficiency of LITA Tg is given by:

$$T_g = \frac{\Lambda}{2\,v_S}.$$

If the fringe spacing Λ is known, the adiabatic-sound velocity v_S in the medium is deduced from T_g. On the other hand, Λ is given by:

$$\Lambda = \frac{\lambda_P}{2\sin\theta}.$$

where λ_P denotes the wavelength of the pump-laser beam and θ the crossing half-angle. For an ideal gas, v_S is related to the temperature by:

$$v_S = \sqrt{\frac{\gamma}{M}RT},$$

where T denotes the temperature, R the molar gas constant, M the molar mass, and γ the specific heat ratio. Therefore, measuring the oscillation period of LITA signal beam intensity indicates the temperature at test volume.

2.4 Numerical analysis of temperature history

Using a hydro code AUTODYN-2D [6,16], we numerically analyzed the shock-induced temperature histories at each observation points with the two-dimensional axisymmetric Euler's equations that are written as:

$$\frac{\partial U}{\partial t} + \frac{\partial F}{\partial x} + \frac{\partial G}{\partial r} + H = 0,$$

where U, F, G, and H denote the state variables and convection fluxes in each direction, respectively, given by

$$U = \begin{pmatrix} \rho \\ \rho u \\ \rho v \\ \rho e \end{pmatrix}, \quad F = \begin{pmatrix} \rho u \\ \rho u^2 + p \\ \rho u v \\ (\rho e + p)u \end{pmatrix},$$

$$G = \begin{pmatrix} \rho v \\ \rho u v \\ \rho v^2 + p \\ (\rho e + p)v \end{pmatrix}, \quad H = \frac{1}{y}\begin{pmatrix} \rho v \\ \rho u v \\ \rho v^2 \\ (\rho e + p)v \end{pmatrix}.$$

Primitive variables in the unknown U are density ρ, velocity components μ and ν, and total energy per unit weight e. Fluid pressure is p and the equation of state for the gas is given by

$$p = (\gamma - 1)\,\rho\,\varepsilon,$$

where ε denotes specific internal energy, and γ, the specific heat ratio, is taken as 1.4. The internal energy is also given by $e = c_V T = RT/(\gamma - 1)$, where c_V denotes the specific heat at constant volume, and R is the gas constant, is taken as 287 J/(kg K). All the calculations were performed in axisymmetric geometry with 0.5 mm square grid. The computational domain used here is shown in Fig. 3. We assumed that the boundary condition of the surface of the shock wave generator was both rigid and adiabatic wall. The energy source of the shock wave was modeled by high-pressure air with an internal energy equal to the discharge energy, 6 J. We allocated a cylindrical region with a diameter of 4 mm and a length of 2 mm for the shock energy source. The initial condition of ambient air was identical to the room environment when the experiment was carried out. In Table 1, the calculation conditions are summarized.
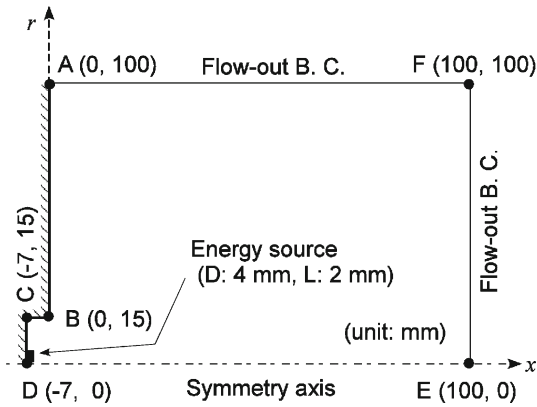
Fig. 3 Schematic diagram of the computational domain

Table 1 Initial condition of numerical analysis

Governing equation	Euler's equations
Mesh interval, Δ	0.5 mm square
Atmosphere	
Equation of state	Ideal-gas
Density, ρ_0	1.225 kg m^{-3}
Specific heat, γ	1.400 (–)
Temperature, T_0	288.2 K
High pressure air	
Total energy, e	6 J
Specific internal energy, e_0	195.1 MJ kg^{-1}
Density, ρ_0	1.225 kg m^{-3}

3 Experimental results

3.1 The characteristics of shock waves

In Fig. 4, both the travel time and the Mach number of the semi-spherical shock waves, generated by high-voltage discharge, show that the shock wave rapidly weakened and reduced its Mach number to near unity with increasing distance. The fitted function [19] of the traveling distance x (m) and the shock Mach number M_S are shown in (1) and (2).

$$x = A + a_0 t + C \ln(1 + a_0 t) + D\sqrt{\ln(1 + a_0 t)} \quad (1)$$

$$M_S = 1 + \frac{C}{1 + a_0 t} + \frac{D}{2(1 + a_0 t)\sqrt{\ln(1 + a_0 t)}} \quad (2)$$

where a_0 (m s^{-1}) is the speed of sound and t (s) time. In the present paper, we determined A, B, and C to be -1.720×10^{-4}, -4.583×10^{-1}, and 1.650×10^{-1}, respectively.

In Fig. 5, pressure histories showed that shock waves were transformed into sonic waves with increasing propagation distance because pressure discontinuity due to shock waves was transformed into moderate change. One can calculate the temperature behind the shock front from the peak pressure ratio P_r^0/P_0 shown in Fig. 5 with two equations delivered by
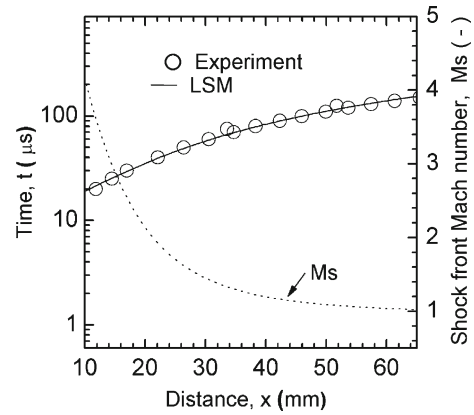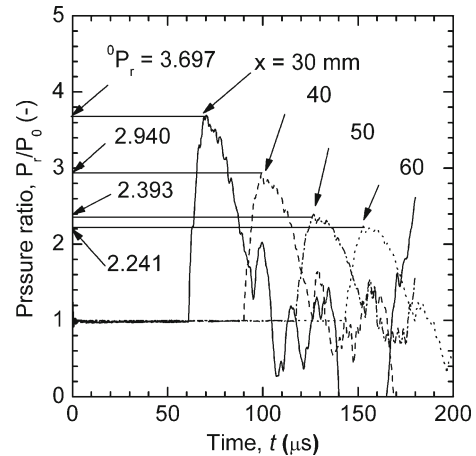

Fig. 4 $x-t$ diagram

Fig. 5 History of measured overpressure

the Rankine–Hugoniot relations, as shown below

$$\frac{T^0}{T_0} = \frac{P_2}{P_0} \cdot \frac{P_2/P_0 + 6}{6(P_2/P_0) + 1}, \quad (3)$$

$$\frac{P_r^0}{P_2} = \frac{9P_2 - P_0}{P_2 + 6P_0}, \quad (4)$$

where T^0 denotes the temperature behind shock waves, T_0, ambient temperature, P_2, the absolute pressure behind shock waves, P_0, atmospheric pressure, and P_r^0, the peak reflected pressure.

Table 2 summarizes the properties of the shock wave based on the experiments here. These results indicate that, at the outermost observed distance, $x = 60$ mm, the shock wave was becoming a very weak shock wave.

3.2 Lens effect on LITA signal

At the moment when the shock front crosses laser beam, the shock front refracts the laser beam. We named this phenomenon lens effect. The mechanism of the lens effect is shown in Fig. 6. The value of laser beam displacement due to the lens

Table 2 Properties of shock wave

	x (mm)			
	30	40	50	60
M_S	1.46	1.19	1.09	1.04
P_r/P_0	3.70	2.94	2.39	2.24
T^0/T_0	1.23	1.18	1.14	1.13
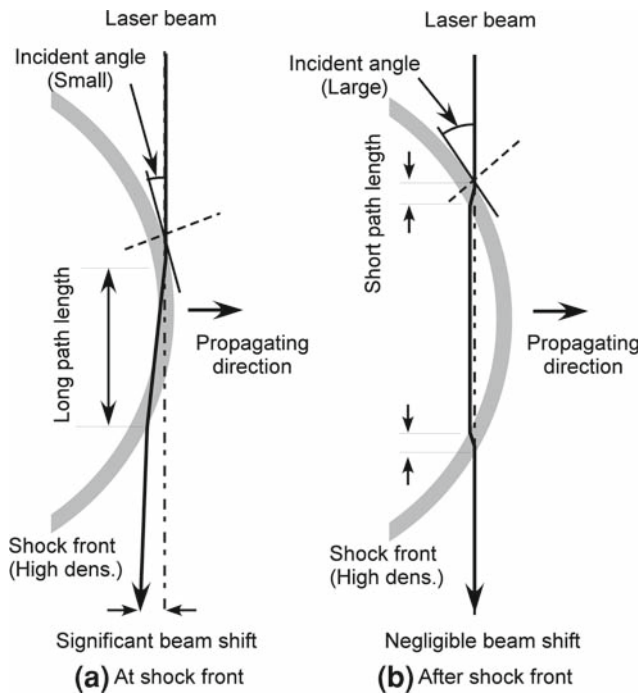
**Fig. 6** Lens effect caused by shock front
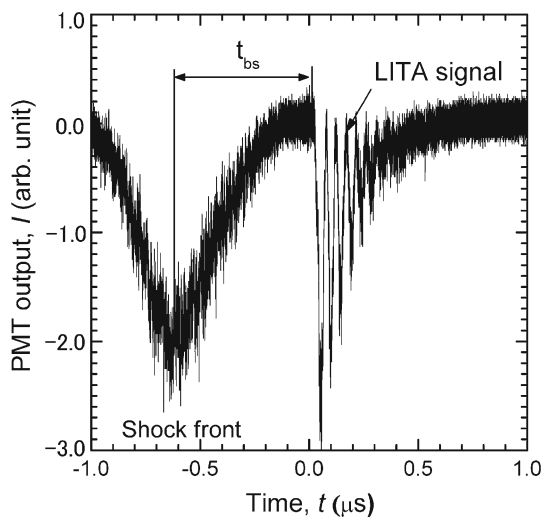
Fig. 7 Typical LITA signal history with shock wave passing

effect is a maximum when the laser beam crosses the shock front because the smaller incident angle provides the larger refraction angle. The LITA signal obtained here showed that

the duration of the lens effect was less than 1 ms. A typical intensity history of a LITA signal that was observed after shock front passage is shown in Fig. 7. The vertical axis indicates the signal beam intensity scaled by an arbitrary unit and the horizontal axis the elapsed time since detection of LITA signal. Before the time $t = 0$, the intensity went down because the deflected probe beam due to the lens effect slotted into the signal path. Although the lens effect bent the path of the signal beam by a small angle when the shock front passed an observed area, the signal retrieved the intensity within 0.5 ms. We assumed that the time, when the peak intensity appeared, indicated the arrival of shock front. Then, the time difference between the peak and $t = 0$, t_{bs} in Fig. 7, indicated the elapsed time from shock front passage in the observed area. Increasing the distance x decreased the magnitude of the intensity changes because the curvature of the shock front decreased. The lens effect was not observed after passage of the shock front on the LITA signal. These results suggest that the lens effect does not interfere with the LITA signal detection except within approximately 1 ms after shock front passage.

3.3 Temperature decay behind shock front

Temperature measurements with LITA were made at distances ranging from 30 to 60 mm with a 10 mm interval. According to the dimension of the shock generator, the shock wave maintained a semi-spherical shape at all distances observed. In Fig. 8, comparison of the temperature ratio T/T_0, determined from LITA signal and from numerical analysis,
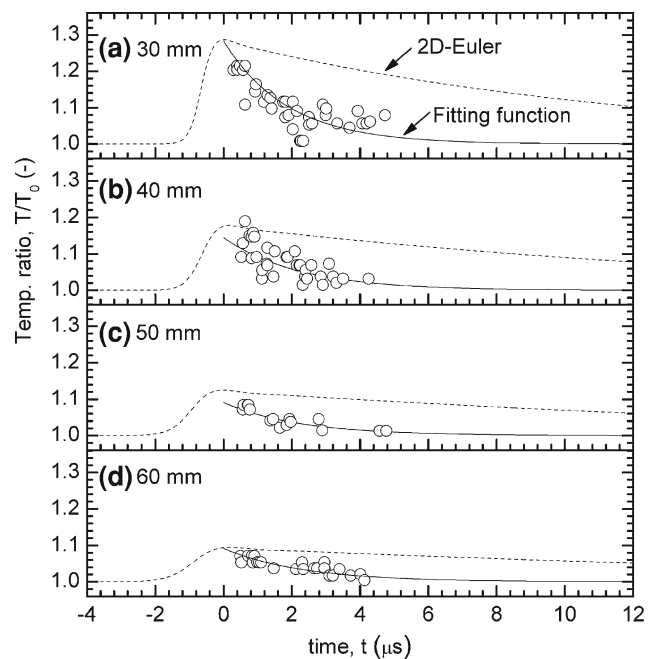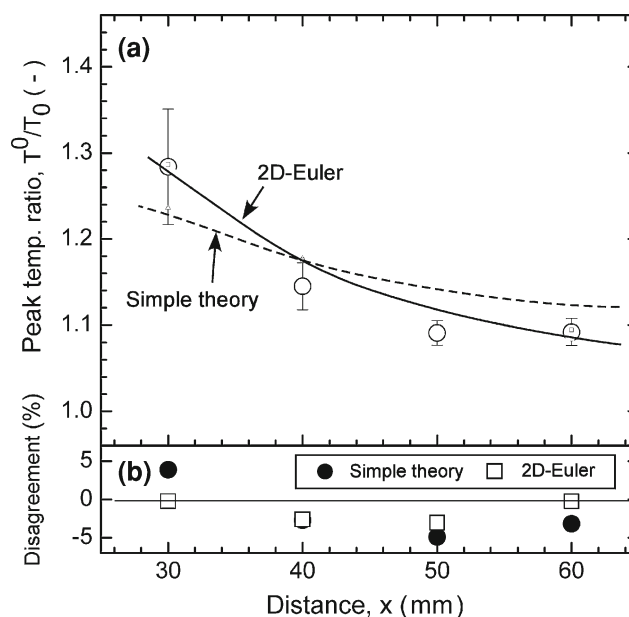

Fig. 8 Temperature decay behind shock front

Table 3 Parameters of the fitting function

	x (mm)			
	30	40	50	60
LITA measurement				
A ($\times 10^{-3}$)	284	145	90.9	91.7
$1/B$ ($\times 10^{-3}$)	536	452	450	432
T^0/T_0	1.28	1.15	1.09	1.09
2D-Euler analysis				
A ($\times 10^{-3}$)	437	426	251	126
$1/B$ ($\times 10^{-3}$)	127	134	112	98.9
T^0/T_0	1.29	1.18	1.13	1.09

Fig. 9 Comparison of peak temperatures behind shock front, Simple theory: the values estimated from observed reflected peak overpressures

showed that the values of peak temperature ratios agreed well; the temperature decay ratio behind the shock wave $1/B$ was less than a quarter of the values in the experiments. T is the absolute temperature determined by the LITA signal, and T_0 is the initial temperature. The open circles refer to experimental results, the solid line to the fitted curves for temperature decay, and the broken lines to the numerical results. The decay was fitted to the exponential function shown in (5).

$$T/T_0 = 1 + A \exp(-t_{bs}/B) \qquad (5)$$

The peak-temperature ratio T^0/T_0 that appeared right behind shock front was estimated using (5). LITA signals indicating T^0/T_0 was superimposed onto the lens effect. Then the values T^0/T_0 were determined by substituting $t = 0$ into (5). Table 3 summarizes the determined parameters A, $1/B$, and T^0/T_0. The temperature ratios T^0/T_0 were in rough agreement with numerical results; the decay rates of the temperature behind the shock front were inconsistent. On the other hand, temperature was determined from internal energy in the numerical analysis, i.e., the behavior of the calculated temperature depends on the pressure. The decay constants of the pressure calculated with Euler's equations should be smaller than that with Navier–Stokes equations. Thus, we concluded that the calculated decay constants were smaller than those in the experiments here. A discussion of the results obtained from the Navier–Stokes equation will be the subject of further study. Regarding the results that were described above, we speculated that the temperature history obtained from the LITA signal disagreed with the calculated value because the numerical analysis neglected the viscosity and considered the specific heat ratio to be constant near the shockfront. Comparing numerical results with different mesh intervals, we verified that the mesh interval used for the calculation was sufficiently fine. Another assumption includes some of other differences that are seen in the decay behind the shock front between the experiment and the numerical method used in this paper. Therefore, for improvement of numerical analysis, we should verify the validity of the values mentioned

above or should change the analysis scheme from 2-D Euler's equations to the point source theory.

3.4 Peak temperature behind the shock front

Figure 9 shows both experimentally obtained peak temperatures and those theoretically estimated. The maximum difference between experiment and theory was 5%. Both the simple theory and 2D-Euler's equations were employed for the estimation. We suspected that the difference between the simple theory and 2D-Euler's equations was caused by the computational domain. The surface of the shock generator was not considered in the simple theory because the simple theory is a one-dimensional calculation; the calculation with 2D-Euler's equations did. Near the electrode, at $x = 30$ and 40 mm, the temperatures obtained with 2D-Euler's equations had higher values than those with the simple theory because reflected shock waves at the partial vacuum of the shock generator would cause an increase of temperature. In contrast, at $x = 50$ and 60 mm, the temperatures obtained with 2D-Euler's equations had lower values than those with the simple theory because diffracted waves decreased the temperatures. LITA measurements agreed with the analysis using 2D-Euler's equations, suggesting that LITA measurements provide accurate peak temperatures behind the shock front.

4 Discussion

One of the medical applications of shock waves: ESWL, which focuses shock waves inside the human organism, has

been successfully applied to calculus disintegration; there has been collateral tissue damage due to induced temperature. The behavior of the temperature caused by shock waves is both unsteady and of short duration. Therefore, thermometry with conventional thermocouples does not have sufficient temporal resolution to analyze the temperature induced by shock waves.

A measurement technique using LITA, allowed us to obtain shock-induced temperatures within 5% error. LITA also obtained temperature histories behind the shock front with sub microsecond temporal resolution. The lens effect that is caused by the shock front passing through the test volume, had a duration of less than 1 μs; the lens effect did not influence the LITA measurements.

Experimentally obtained temperature-decay rates were approximately four times larger than those of numerical results given by the 2-D Euler's equations. The non-viscosity treatment of the flow field in numerical analysis affected the difference of temperature-decay rates behind the shock front. In the present paper, the effect of viscosity on temperature decay remained unclear.

The experimental results shown in this paper indicated that LITA must be an effective technique for temperature measurement behind a shock front propagating in air. Then, LITA has applicability to temperature measurements for underwater shock waves of ESWL.

5 Conclusions

We applied LITA to non-intrusive thermometry for shock-induced phenomena, and tried to obtain the temperature distributions behind spherical shock waves generated by high-voltage discharges in the air. The temperature profile behind the shock front was successfully obtained at every 10 mm, for distances ranging from 30 to 60 mm from the electrode. Signal beam refraction caused by the passing of a shock front at the test volume had limited effect on LITA signal acquisition. The peak-temperature ratios determined by LITA signals agreed with the results of numerical analysis and peak overpressure experiments. The differences among them were within 5%. The temperature-decay constants determined by LITA signals were over four times larger than those by numerical analysis. The scattered values of the temperature history behind the shock front suggested that complex flows occurred behind the shock front. Improvement in measurement stability is required for the LITA method. The paper examined relatively weak shock waves in the air; medical applications are usually carried out underwater and with strong shock waves. We will investigate the accuracy of temperature measurement with LITA for strong shock waves and underwater shock waves.

References

1. Adelgren, R.G., Elliott, G.S., Knight, D.D., Zheltovodov, A.A., Beutner, T.J.: Energy deposition in supersonic flows. AIAA Paper 2001-0885 (2001)
2. Adelgren, R.G., Elliott, G.S., Crawford, J.B., Carter, C.D., Grosjean, D., Donbar, J.M.: Axisymmetric jet shear layer excitation induced by electric arc discharge and focused laser energy deposition. AIAA Paper 2002-0729 (2002)
3. Adelgren, R.G., Yan,H., Elliott, G.S., Knight, D., Buetner, T., Zheltovodov, A., Ivanov, M., Khotyanovsky, D.: Localized flow control by laser energy deposition applied to Edney IV shock impingement and intersecting shocks. AIAA Paper 2003-0031 (2003)
4. Alderfer, D.W., Herring, G.C., Danehy, P.M., Mizukaki, T., Takayama, K.: Submicrosecond temperature measurement in liquid water with laser-induced thermal acoustics. Appl. Opt. **44**, 2818–2826 (2005)
5. Aradag, S., Yan, H., Knight, D.: Energy deposition in supersonic cavity flow. AIAA Paper 2004-0514 (2004)
6. Century Dynamics, Inc.: AUTODYN Electronic Document Library. Century Dynamics Inc. (1997)
7. Chaussy, Ch., Schmiedt, E., Jocham, D., Walther, V., Brendel, W., Forssmann, B., Hepp, W.: Extracorporeal Shock Wave Lithotripsy. Karger, Basel (1982)
8. Cords, P.H. Jr.: A high resolution, high-sensitivity color schlieren method. In: The 12th SPIE technical symposium, pp. 85–88 (1968)
9. Eichler, H.J., Günter, P., Pohl, D. W.: Laser-induced Dynamic Gratings. Springer, Berlin (1986)
10. Glumac, N., Elliot, G., Boguszko, M.: Temporal and spatial evolution of a laser spark in air. AIAA J. **43**, 1984–1994 (2005)
11. Gojani, A.B., Danehy, P.M., Alderfer, D.W., Saito, T., Takayama, T.: Development of laser-induced grating spectroscopy for underwater temperature measurement in shock wave focusing regions. SPIE International Symposiumon Optical System Design, Saint-Etiennes, France (2003)
12. Gordeev, V.P., Krasilnikov, A.V., Lagutin, V.I., Otmennikov, V.N.: Experimental study of the possibility of reducing supersonic drag by employing plasma technology. Izvestiya RAS Mekhanica Zhidkosti Gaza **31**, 177–182 (1996)
13. Hart, R.C., Balla, R.J., Herring, G.C.: Simultaneous velocimetry and thermometry of air by use of non resonant heterodyned laser-induced thermal acoustics. Appl. Opt. **40**, 965–968 (2001)
14. Hart, R.C., Herring, G.C., Balla, R.J.: Common-path heterodyne laser-induced thermal acoustics for seedless laser velocimetry. Opt. Lett. **27**, 710–712 (2002)
15. Kuwahara, M., Ioritani, N., Kambe, K., Orikasa, S., Takayama, K.: Anti-miss-shot control device for selective stone disintegration in extracorporeal shock wave lithotripsy. Shock Waves **1**, 145–148 (1991)
16. Katayama, M., Toda, S., Kibe, S.: Numerical simulation of space debris impacts on the whipple shield. Acta Astron. **12**, 859–869 (1997)
17. Kilmov, A.I., Koblov, A.N., Mishin, G.I., Serov, Y.L., Yavor, I.P.: Shock wave propagation in a glow discharge. Sov. Tech. Phys. Lett. **8**, 192–194 (1986)
18. Kleine, H., Grönig, H.: Color schlieren methods in shock wave research. Shock Waves **1**, 51–63 (1991)

19. Kleine, H., Dewey, J.M., Ohashi, K., Mizukaki, T., Takayama, K.: Studies of the TNT equivalence of silver azide charges. Shock Waves **13**, 123–138 (2003)

20. Kunauss, H., Roediger, T., Gaisbauser, U., Karaemer, E., Bountin, D.A., Smorodsky, B.V., Maslov, A.A., Srulijes, J., Seiler, F.: A novel sensor for fast heat measurements. Collect. Tech. Pap. 25th AIAA Aerodyn. Meas. Technol. Ground Test Conf., vol. 2, pp. 1054–1085 (2006)

21. Kolesnichenko, Y., Brovkin, V., Azarova, O., Grudnitsky, V., Lashkov, V., Mashek, I.: MW energy deposition for aerodynamic application. AIAA Paper 2003-0362 (2003)

22. Kozlov, D.N., Hemmerling, B., Stampanoni-Panariello, A.: Measurement of gas jet flow velocimetries using laser-induced electrostrictive gratings. Appl. Phys. B **71**, 585–591 (2000)

23. Kuwahara, M., Kambe, K., Kurosu, S., Orikasa, S., Takayama, K.: Extracorporeal stone disintegration using chemical explosive pellets as an energy source of underwater shock waves. J. Urol. **135**, 814–817 (1986)

24. Macheret, S.O., Shneider, M.N., Miles, R.B.: Scramjet inlet control by iff-body energy addition: a virtual cowl. AIAA Paper 2003-0032 (2003)

25. Marconi, F.: An investigation of tailored upstream heating for sonic boom and drag reduction. AIAA Paper 98-0333 (1998)

26. Poggie, J.: Energy addition for shockwave control. AIAA Paper 99-3612 (1999)

27. Satheesh, K., Jagadeesh, G.: Effect of concentrated energy deposition on the aerodynamic drag of a blunt body in hypersonic flow. Phys. Fluids **19**, 031701-1–031701-4 (2007)

28. Schlamp, S., Cummings, E.B., Sobota, T.H.: Laser-induced thermal-acoustic velocimetry with heterodyne detection. Opt. Lett. **25**, 224–226 (2000)

29. Takayama, K.: Application of underwater shock wave focusing to the development of extracorporeal shock wave lithotripsy. Jpn. J. Appl. Phys. **32**, 2192–2198 (1993)

30. Walker, D.J.W., Williams, R.B., Ewart, P.: Thermal grating velocimetry. Opt. Lett. **23**, 1316–1318 (1998)

31. Yan, H., Adelgren, R.G., Elliott, G.S., Knight, D., Buetner, T.: Effect of energy addition on MR to RR transition. Shock Waves **13**, 113–121 (2003)

32. Zaidi, S.H., Shneider, M.N., Mansfield, D.K., Ionikh, Y.Z., Miles, R.B.: Influence of upstream pulsed energy deposition on a shock-wave structure in supersonic flow. AIAA Paper 2002-2703 (2002)